water

MDPI

Article

A Mesoporous Faujasite Prepared by Space-Confined Method for Highly Effective Selectivity of Copper Ions

Yi Chen [1], Shiyue Wei [1], Shuai Dong [1], Jinchuan Gu [1,*] and Wenju Jiang [2]

[1] School of Food and Bioengineering, Civil Engineering and Architecture and Environment, Xihua University, Chengdu 610039, China; evechen1@163.com (Y.C.); wsykkky@163.com (S.W.); ds2567033821@163.com (S.D.)
[2] College of Architecture and Environment, Sichuan University, Chengdu 610065, China; wenjujiang@scu.edu.cn
* Correspondence: gu6471@163.com; Tel.: +86-28-8772-0549

Abstract: The discharge of copper ion (Cu(II)) into natural waters can lead to serious environmental and health problems; however, an abundantly porous hierarchical adsorbent, such as faujasite (FAU), can rapidly remove unwanted Cu(II). In this research, a hierarchically structured, abundantly mesoporous faujasite (FAU) was fabricated from industrial-waste lithium-silicon powder (LSP), with the addition of biochar and graphene oxide (GO) via hydrothermal synthesis without high-temperature calcination. The results demonstrated that just a small amount of biochar or GO can significantly improve the mesopore volume (0.14 cm^3/g) and the Cu(II) adsorption capacity (115.65 mg/g) of composite FAU. In particular, careful examination of the properties of the composite FAU showed that the biochar and GO had favorably affected the growth of the zeolite crystals, thus promoting the formation of the FAU skeleton structure, ion-exchange sites and Si-OH. The composite FAU exhibited superior adsorption capacities and highly effective Cu(II) selectivity. Thus, the findings of this study provide a novel and cost-effective avenue for the synthesis of composite FAU with high copper-selective removal capacity.

Keywords: adsorption; copper ion; faujasite; hierarchical structure; mesoporous; selectivity

Citation: Chen, Y.; Wei, S.; Dong, S.; Gu, J.; Jiang, W. A Mesoporous Faujasite Prepared by Space-Confined Method for Highly Effective Selectivity of Copper Ions. *Water* **2022**, *14*, 2040. https://doi.org/10.3390/w14132040

Academic Editors: Ewa Okoniewska, Małgorzata Worwąg and Mariusz Kowalczyk

Received: 9 May 2022
Accepted: 24 June 2022
Published: 25 June 2022

1. Introduction

Copper (Cu) is used widely in many diverse industries, from infrastructure, mining, steel production and transportation, to the manufacture of electronic equipment and various finishing processes [1,2]. The demand for and utilization of Cu has grown rapidly in recent decades as a result of global economic growth [1], which has significantly increased the amount of residual copper (mainly copper ions) being deposited in industrial wastewater, and thence into the natural environment. Since copper ion (Cu(II)) is a biotoxic heavy-metal ion, its presence in natural water can lead to serious environmental and health problems and it can diffuse easily from a water environment into various systems throughout the ecosystem, such as particulate matter in the air [3], soil [4], riverbeds [5,6] and marine sediments [7], resulting in widespread potential harm. Therefore, not only is it essential to control the Cu(II) discharge from various sources into the ecosystem, but the already present accumulation of Cu(II) must also be effectively removed.

Numerous technologies are currently used to remove Cu(II) from water, including chemical precipitation [8–10], membrane separation [11], electrochemical means [12,13] and adsorption [14–16]. Compared with chemical precipitation, the adsorption method has a wider range of applications, does not generate secondary pollution and the adsorbent after adsorption can also be recycled. The adsorption method also has broader application conditions than both the membrane-separation and electrochemical methods, along with high removal efficiency, low cost and large-scale suitability. The key to the adsorption method is its choice of adsorbent, and therefore, the development of a low-cost, highly efficient Cu(II) adsorbent has garnered increasing global attention.

Zeolite is used extensively for the removal of Cu(II) from water [17–19], and hierarchical faujasite (FAU), a type of zeolite with a hierarchical porous structure that is both microporous and meso/macroporous [20], has proven to be especially effective for this purpose [16,17]. FAU is formed by corner-sharing a silicon/aluminum oxygen tetrahedron with interconnected multielement rings to form a network of cavities [17]. This highly porous structure features 'supercages' of a 1.3 nm diameter and interconnected pores of 0.74 nm [21], which provide sufficient active sites for separation and catalytic processes. However, the small pore size of 1.3 nm also limits the diffusion of reactants in these zeolite crystals. Previous literature has proposed mechanisms for Cu(II) adsorption by FAU that include physical interception, ion exchange, electrostatic attraction and/or hydroxyl complexation, but these have confirmed that pore diameter is an important factor affecting the successful removal of Cu(II) [17]. FAU with wide pores and/or a short diffusion length has been shown to achieve higher mass-transfer efficiency [22,23], and mesopores are considered key to the mass-transfer process [24,25]. Hence, mesopores can improve the diffusion rate as well as the accessibility of micropores inside the zeolite to effectively improve the Cu(II) adsorption performance of FAU [22,26].

Space-confined synthesis is an effective method through which to realize control of the structure and size of zeolites by introducing an inert matrix into different channels or crystal gaps that can confine the direction of crystal growth. According to previous studies, this method can effectively improve the mesoporosity of FAU, and thus promote the mass-transfer process within its pores [27]. Carbon has been widely used as the inert matrix in this approach, and the ideal hierarchical porosity of zeolite has reportedly been obtained by calcinating the carbon at high temperature [26,28,29]. However, these methods require high-temperature calcination to remove the carbon in order to produce new pores, a requirement that not only wastes the carbon materials but also consumes energy and generates greenhouse gases. Therefore, the development of an environmentally friendly, energy efficient and simple approach to space-confined synthesis is crucial.

In this study, we propose the use of a very small amount of biochar and graphene oxide (GO) to improve FAU performance through space-confinement without calcination. Industrial-waste lithium-silicon powder (LSP) was used as FAU raw material, which greatly reduced the preparation cost, and in addition, utilized a waste resource. The surface chemical properties and pore structure of the biochar were modified via different methods, and the influence of the surface properties of both biochar and GO on FAU were examined. Finally, the Cu(II) adsorption performance and selective adsorption capacity of the composite FAU were evaluated.

2. Materials and Methods

2.1. Materials

The LSP and walnut shell used in this study were obtained from China Lithium Products Technology Co., Ltd. (Chengdu, China) and a local market, respectively. LSP is comprised mainly (wt.%) of O (57.67%), Si (22.26%), Al (9.46%), Ca (3.62%), S (3.60%), Fe (0.67%), K (0.31%) and trace amounts (0.008–0.16%) of Na, P, Mg, Rb and Mn, among others. Phosphoric acid (H_3PO_4), copper nitrate ($Cu(NO_3)_2{\cdot}3H_2O$), 67% nitric acid (HNO_3), sodium hydroxide (NaOH), sodium aluminate ($NaAlO_2$), sodium silicate ($Na_2SiO_3{\cdot}9H_2O$), sodium chloride (NaCl) and sodium acetate ($CH_3COONa{\cdot}3H_2O$) were purchased from Chengdu Kelong Chemicals Co., Ltd. (Chengdu, China). GO was prepared by Hummers' method [30], with a surface area and average pore diameter of 7 m^2/g and 6.44 nm, respectively.

2.2. Synthesis of Composite Zeolite

Walnut shell biochar (WSB) was prepared by mixing the walnut shell powder with H_3PO_4 (weight ratio 1.94:100) via pyrolysis in a microwave oven under N_2 flow at 500 W for 530 s. Thereafter, 10 g WSB was modified with 100 mL 67% HNO_3 (H-WSB) and 200 mL 0.5 M NaOH (N-WSB), respectively, and stirred at 353 K until dry. The H-WSB modified with NaOH according to the above method was subsequently designated as HN-WSB. The

samples were washed with deionized water until a neutral pH was reached, whereafter they were dried at 378 K.

The FAU zeolite (Z) was prepared via hydrothermal synthesis, with a Si/Al ratio of 9, according to the following processes [17]: LSP was treated with 1 mol/L HCl (H-LSP); 6 g H-LSP and 16.07 g $Na_2SiO_3 \cdot 9H_2O$ were mixed with NaOH solution (3 g NaOH/20 mL deionized water). The mixture was aged for 12 h, then hydrothermally treated under 373 K for 15 h. The samples were washed with deionized water and dried at 378 K.

The biochar/GO composite FAU was denoted as WSB-Z/H-WSB-Z/N-WSB-Z/HN-WSB-Z/GZ, of which WSB/H-WSB/N-WSB/HN-WSB/GO was added to the mixed solution. The HN-WSB-Z and GZ were prepared by introducing 0.05–0.5 g (2.5–25 g/L) of HN-WSB and 0.01–0.1 g (0.5–5 g/L) of GO into the gel before hydrothermalization, whereafter the follow-up work was performed as per the preparation of Z to obtain *x*HN-WSB-Z and *y*GZ, where *x* and *y* refer to the HN-WSB and GO addition per unit volume solution.

2.3. Physical Characterization

N_2 adsorption–desorption isotherms were collected on a surface area, whereafter porosity analysis (Micromeritics ASAP 2460, Micromeritics, Georgia, USA) was performed at −77 K, and the specific surface area (S_{BET}) and micropore volume (V_{mic}) of the samples were calculated via the Brunauer–Emmett–Teller (BET) and t-plot method, respectively, while the mesopore volume (V_{mes}) and mesopore-size distribution were determined via the BJH equation. X-ray diffraction (XRD) patterns were obtained using an Empyrean diffractometer (Malvern Panalytical Ltd., Malvern, UK) with CuK_α radiation (0.02°/s). The surface morphologies and elemental components were obtained via scanning electron microscopy (SEM) (JSM-7500F, JEOL, Tokyo, JPN), while Fourier-transform infrared (FTIR) spectroscopy was performed using an infrared spectrophotometer (Nicolet 6700, Thermo Fisher Scientific, Waltham, MA, USA), and X-ray photoelectron spectroscopy (XPS) was conducted on an AXIS Ultra DLD spectrometer (Kratos Analytical Ltd., Manchester, UK).

2.4. Metal-Ion-Adsorption Experiments

Stock solutions (1 g/L) of Cu(II), Ca(II), Mn(II), Ni(II), Co(II) and Mg(II) were prepared by dissolving $Cu(NO_3)_2 \cdot 3H_2O$, $Ca(NO_3)_2 \cdot 4H_2O$, $Mn(NO_3)_2$(50 wt.% in H_2O), $Ni(NO_3)_2 \cdot 6H_2O$, $Co(NO_3)_2 \cdot 6H_2O$ and $Mg(NO_3)_2 \cdot 6H_2O$ in deionized water. Thereafter, metal-ion solutions were prepared using appropriate dilutions of the stock solutions. The Cu(II) adsorption behaviors of the prepared samples were estimated via batch adsorption experiments. Each sample was poured into a 250 mL Erlenmeyer flask containing 50 mL Cu(II) solution (20 mg/L) and the mixture was shaken in an isothermal vibrator (298 K) for 180 min. This solution was then filtrated through a 0.45 μm membrane filter and measured by means of an atomic absorption spectrophotometer (AAS, AA-6880, Shimadzu Corporation, Kyoto, Japan). The selective adsorption experiments were carried out in batch single-metal solutions, Cu(II)-containing two-component metal-ion solutions and multicomponent metal-ion coexisting solutions, with 20 mg/L concentration of each type of metal ion. All adsorption experiments were carried out in triplicate.

2.5. Reusability Experiment

A sample (0.15 g) was added to 750 mL Cu(II) solution (10 mg/L) and the mixture was shaken in an isothermal vibrator (298 K) for 180 min. This solution was then filtrated through a 0.45 μm membrane filter, and the concentration of Cu(II) in the filtrate was measured via AAS at 324.7 nm. The used sample was regenerated by being washed continuously with a saturated sodium chloride/2M sodium acetate/hot (333 K) deionized water solution until no Cu(II) was detected in the filtrate. The sample was subsequently washed with deionized water and dried at 378 K before the next adsorption experiment.

3. Results and Discussion

3.1. Effect of Biochar and GO on Crystallization of FAU

3.1.1. Textural Properties

The N_2 adsorption–desorption isotherms of the samples are presented in Figure 1, in which it can be seen that WSB and N-WSB presented type IV isotherms (IUPAC system), indicating the existence of mesopores (Figure 1a), further verified by pore-size distribution (Figure 1e). Both H-WSB and HN-WSB presented poor pore structures (Figure 1a), with pore volumes significantly lower than those of WSB and N-WSB (Figure 1e). The textural parameters of the different samples are summarized in Table 1. WSB and N-WSB showed high S_{BET} (1032 and 1236 m^2/g, respectively) and total pore volume (V_{tot}, 0.74 and 0.97 cm^3/g, respectively). In Figure 1b, it is evident that the N_2 adsorption capacities of biochar composite FAUs were affected slightly by different biochars; however, the pore volumes, especially those of V_{mes}, were significantly increased compared with those of Z (Figure 1f). It should be noted that the V_{mes} of HN-WSB-Z prepared by HN-WSB showed the greatest increase (0.11 cm^3/g), while the N-WSB-Z prepared by N-WSB underwent the smallest change (0.01 cm^3/g). This indicates that the pore structure of the biochar, when added in small amounts, had little effect on the structure of the synthesized FAU. In Figure 1c, it is evident that the N_2 adsorption capacities of GZ were slightly changed by the addition of GO. The pore volumes increased significantly (Figure 1g), with the V_{tot} and V_{mes} increasing 0.13 cm^3/g and 0.14 cm^3/g (Table 1), respectively. The above results indicate that HN-WSB and GO can significantly improve the mesoporous ratio of composite FAU.

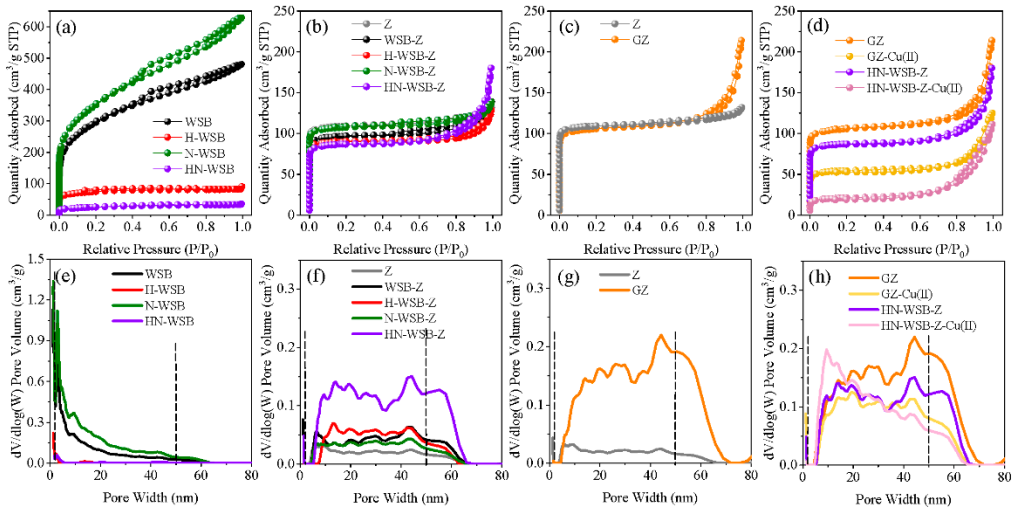

Figure 1. The N_2 adsorption–desorption isotherm of different biochars (**a**), different biochar composite FAUs (**b**), GO composite FAU (**c**), composite FAUs after adsorbing Cu(II) (**d**), and the corresponding pore-size distributions (**e**–**h**).

As the diameter of copper hydration ions are greater than 0.838 nm, they can be physically trapped by an adsorbent with diameters 1.3–1.8 times larger (1.089–1.508 nm) [17,31]. After adsorbing Cu(II), the S_{BET} of HN-WSB-Z-Cu(II) and GZ-Cu(II) were found to have decreased to 209 and 163 cm^2/g, respectively, while the V_{mic} significantly decreased to 0.02 and 0.07 cm^3/g, indicating the occupation of micropores by Cu(II). There was a slight decrease in V_{mes}, indicating that Cu(II) had been retained in the mesoporous channels. These results are attributed to the rapid diffusion and physical capture of copper ions in FAU zeolite crystal cages due to the highly porous structure.

Table 1. Textural properties of different samples.

Samples	S_{BET}	V_{tot}	V_{mic}	V_{mes}
	m^2/g	cm^3/g	cm^3/g	cm^3/g
WSB	1032	0.74	0.08	0.66
H-WSB	243	0.14	0.07	0.07
N-WSB	1236	0.97	0.10	0.87
HN-WSB	87	0.05	0.01	0.04
Z	347	0.20	0.15	0.05
WSB-Z	307	0.22	0.14	0.08
H-WSB-Z	284	0.20	0.13	0.07
N-WSB-Z	342	0.21	0.15	0.06
HN-WSB-Z	278	0.28	0.12	0.16
HN-WSB-Z-Cu(II)	69	0.17	0.02	0.15
GZ	337	0.33	0.14	0.19
GZ-Cu(II)	174	0.19	0.07	0.12

S_{BET}: BET surface area; V_{tot}: total pores volume; V_{mic}: micropore volume; V_{mes}: mesopore volume.

The SEM image of HN-WSB-Z in Figure 2a shows that the zeolite particles are stacked together, and that the crystal gap formed some pores. Compared with Z (Figure S1), the crystal gap of HN-WSB-Z increased, which may be related to the fact that the addition of HN-WSB-Z promoted the increase in mesopores/macropores. Figure 2c shows the thin laminated structure of GO with slight folds. In Figure 2b,d, it is evident that the zeolite particles were inlaid with GO in the GZ structure, while the mapped elements (Figure 2e) also confirmed the compound structure of GZ.

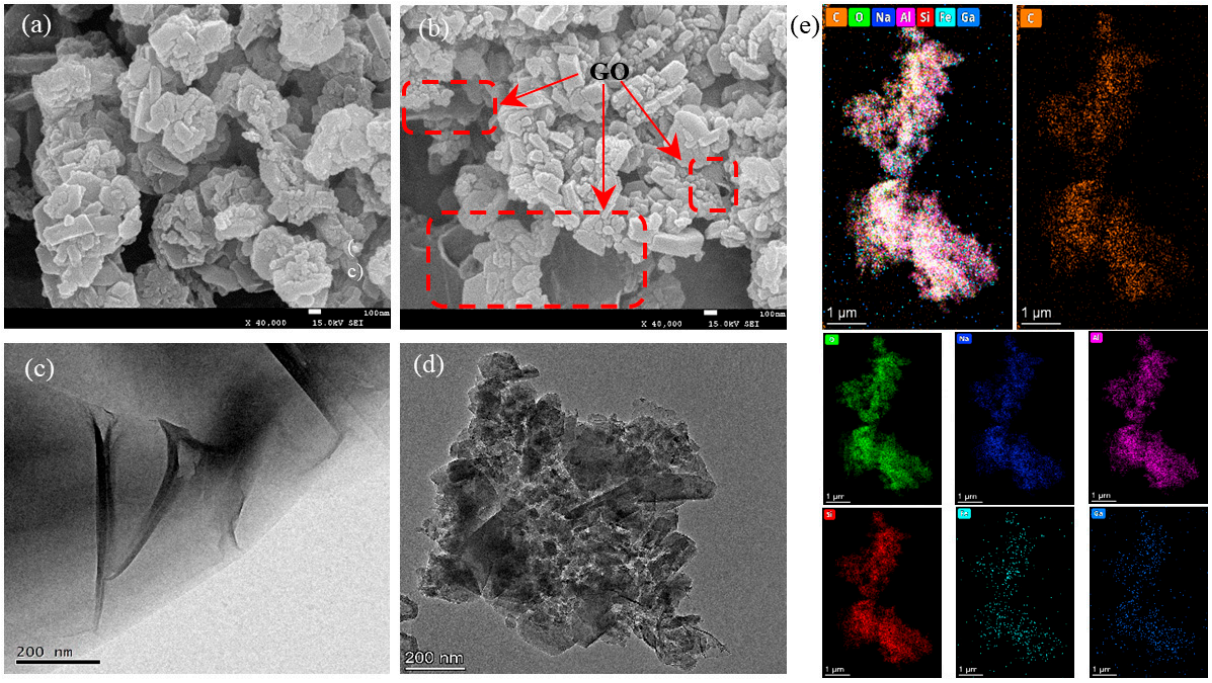

Figure 2. SEM images of HN-WSB-Z (**a**) and GZ (**b**), TEM images of GO (**c**) and GZ (**d**), and the element-mapping analysis of GZ (**e**).

3.1.2. XRD Analysis

Figure 3 illustrates the XRD patterns of the different biochars, GO and composite FAUs. It can be seen from Figure 3a that none of the different kinds of biochar have a significant characteristic peak, which suggests that they are all amorphous. The GO showed a characteristic peak located at 9.985°, and the GO layer spacing was calculated via Bragg's Law to be 8.85 Å, which is significantly larger than graphite layer spacing (3.370 Å, Figure S2). This indicates that the GO was highly oxidized due to the layer spacing being

directly proportional to its degree of oxidation [32,33]. The highly oxidized and large layer spacing of GO may be beneficial to the space confinement and structure induction of zeolite.

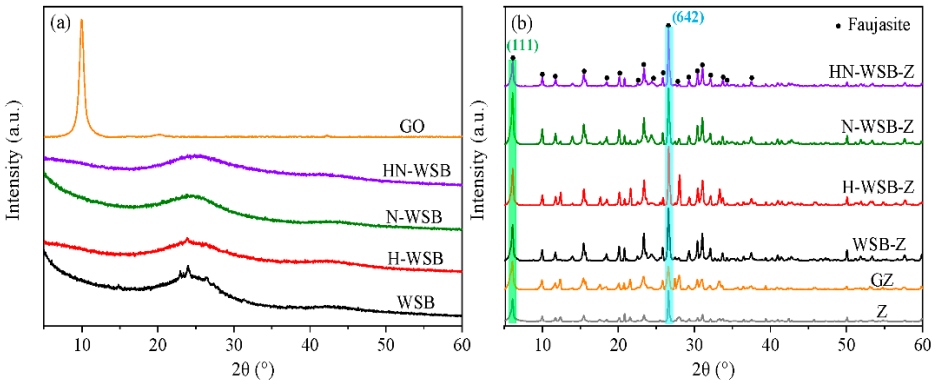

Figure 3. XRD patterns of GO and different biochars (**a**); GO composite FAU, different biochar composite FAUs and pure FAU (Z) (**b**).

Figure 3b shows that all the composite zeolites in this study presented similar XRD patterns, indicating pure FAU (JCPDS No. 38-0238) [17,34]. These results indicate that the purity of FAU was not affected by the involvement of biochar and GO in the crystals. Compared with Z, the FAU characteristic peaks of all composite FAUs were significantly enhanced, thus confirming that the addition of biochar and GO does, indeed, promote the growth of zeolite crystals.

The main diffraction peaks of FAU at 6.176° and 26.930° correspond to the lattice plane (111) and (642). The crystallite dimensions (CD) of the composite FAUs with main lattice planes of (111) and (642) are shown in Table S1, as calculated using the Scherrer equation. HN-WSB-Z had the maximum CD value at the (642) lattice plane, and the CD value of its (111) lattice plane was slightly increased compared with that of Z, indicating that HN-WSB-Z growth had occurred mainly along the crystal plane perpendicular to (642). The CD value of GZ at the (111) lattice plane had increased, but the CD value of its (642) lattice plane had decreased, indicating that GZ grew mainly along the crystal plane perpendicular to (642).

3.1.3. Surface Chemistry

The FTIR spectra of the biochar, GO and composite FAUs are summarized in Figure 4. The FTIR spectra of pristine GO show three characteristic peaks, located at 1056 cm^{-1}, 1583 cm^{-1} and 1719 cm^{-1}, corresponding to C-O-C stretching, O-C=O stretching and C=O stretching, respectively [35,36].The band at around 3400 cm^{-1}, representing the existence of O-H functional groups, was observed in both the biochar and GO (for example, -OH and -COOH) [37], while the peak at approximately 1576 cm^{-1} of the biochar was attributed to the vibration of -C-O/C-O-C [37]. Furthermore, the observable peaks at 1707, 1527,1335 and 1243 cm^{-1} were attributed to the vibration of aromatic C=O/C=O (for example, COOH) [37,38], -C-O/C-O-C [37], lactonic [39,40] and phenolic C-O/-COOH [41] functional groups, which were detected only in HN-WSB, indicating that the NaOH-HCl modification increased the oxygen-containing functional groups on the surface of WSB. The abundant oxygen-containing functional groups on the surface of GO and HN-WSB are beneficial as they attract substances such as aluminosilicate and help to induce their directional growth along the surface [42,43], thereby achieving the purpose of enhanced mesoporosity and improved FAU performance.

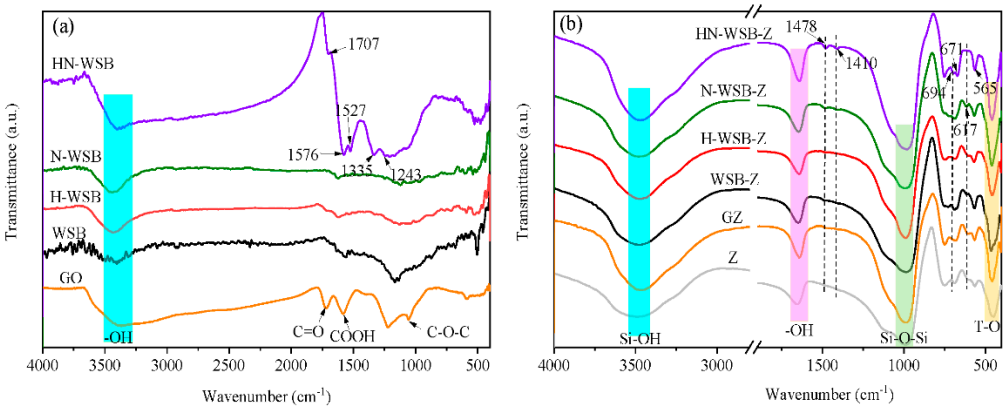

Figure 4. FTIR spectra of GO and different biochars (**a**); GO composite FAU, different biochar composite FAUs and pure FAU (**b**).

In the FTIR spectra (Figure 4) of the composite FAUs, it is evident that the peaks at approximately 3472 and 1642 cm^{-1} corresponded to the -OH groups related to zeolitic structures and those of interstitial bonded water, respectively [44,45]. The band at approximately 1000 cm^{-1} can be attributed to the antisymmetric stretching vibration of Si-O-Si [44], while those in the region of 420–500 cm^{-1} were assigned to the internal bending vibrations of T-O (T = Si, Al) in tetrahedra [44–46]. The intensity of the abovementioned peaks (Si-OH, -OH, Si-O-Si and T-O) increased significantly after the introduction of biochar and GO in Z, indicating that the carbon material strengthens the structure of zeolites. The peaks situated at 751 cm^{-1} are attributed to the symmetrical stretching of T-O bonds (T = Si or Al) [47], while the band at approximately 671 cm^{-1} is associated with the internal symmetric stretching of T-O-T (T = Al or Si) [48]. The bands between 617 and 565 cm^{-1} are related to the D6R formation of the FAU framework [49,50], and the intensity of the peak at 565 cm^{-1} was clearly enhanced in the composite zeolites. The peaks detected only in HN-WSB-Z and N-WSB-Z at 1478 cm^{-1} and 1410 cm^{-1} belong to the external asymmetric stretching of T-O-T and the ring-stretching vibration, respectively [48,51]. In particular, the band around 694 cm^{-1}, which belongs to the symmetric stretching of T-O-T, was seen only in HN-WSB-Z [48], which indicates that the addition of HN-WSB promoted the formation of the T-O-T structure.

As can be seen from Figure S3, the peaks at approximately 3478 and 1642 cm^{-1} on HN-WSB-Z and GZ shifted to 3425 (3428) and 1640 (1639) cm^{-1} on HN-WSB-Z-Cu(II) and GZ-Cu(II), respectively, indicating that the adsorption process is related to -OH [17,46].After the adsorption of Cu(II) (Figure S3a), the peaks at 1410, 751 and 671 cm^{-1} shifted to 1385, 758 and 685 cm^{-1}, respectively, while the peaks at 1478 cm^{-1} disappeared, two additional peaks were detected at 725 and 685 cm^{-1} on HN-WSB-Z-Cu(II), and the peak at 565 cm^{-1} shifted to 590 cm^{-1} on GZ-Cu(II). The above changes in the peaks were all caused by the stretching of T-O-T [44,52], indicating that the adsorption of Cu(II) resulted in a slight distortion of the zeolite skeleton. This may have been due to the exchange of sodium ions for copper ions and/or the attraction of the silicon/aluminum-oxygen tetrahedral charge [17]. The T-O-T structure of the FAU was enhanced through the addition of carbon materials, which is beneficial to the electrostatic attraction of Cu(II).

The binding energies and relative contents of elements in the different carbon material and zeolites by XPS are presented in Table 2. The surface of biochar was found to be composed mainly of C and O, while the Na was found only in HN-WSB and N-WSB (Figure S4a), possibly introduced through the NaOH modification. Na concentrations were approximately 6.70% and 1.39% (Table 2) in the HN-WSB and N-WSB, respectively, which may be beneficial to the formation of zeolite ion-exchange sites. The survey spectra of Z were seen to contain peaks centered at 1072.2, 531.8, 102.2 and 74.7 eV for Na (1s), O (1s), Si (2p) and Al (2p), respectively (Figure S4b). These peaks observably shifted following the introduction of biochar and GO (Table 2). The composite FAUs' binding energy of O

(1s), Si (2p) and C (1s) shifted to a higher energy compared with Z and the corresponding carbon material, suggesting that the zeolite experienced a strong interaction with the C in carbon material [53,54]. In addition, the Na relative contents of the biochar composite FAUs elements were enhanced approximately 0.88–1.82% than that of Z, indicating that biochar can promote the generation of ion-exchange sites.

Table 2. The binding energy (eV) and relative content (wt.%) of elements of different carbon materials and zeolites via XPS.

Samples	C	O	Si	Al	Na	Cu
GO	(66.25%)	(33.75%)	-	-	-	-
WSB	284.5 (81.13%)	533.1 (18.87%)	-	-	-	-
H-WSB	285.0 (69.93%)	533.1 (30.07%)	-	-		-
N-WSB	284.7 (86.29%)	532.9 (12.32%)	-	-	1071.7 (1.39%)	-
HN-WSB	284.9 (64.51%)	532.4 (28.79%)	-	-	1071.6 (6.70%)	-
Z	-	531.8 (57.63%)	102.2 (23.55%)	74.7 (10.51%)	1072.2 (8.31%)	-
WSB-Z	285.4 (10.13%)	531.9 (50.16%)	102.3 (20.39%)	74.6 (8.98%)	1072.4 (10.13%)	-
H-WSB-Z	285.3 (15.52%)	532.0 (47.47%)	102.3 (18.63%)	74.6 (9.05%)	1072.3 (9.33%)	-
N-WSB-Z	285.1 (13.30%)	531.8 (48.05%)	102.3 (20.38%)	74.2 (9.08%)	1072.0 (9.19%)	-
HN-WSB-Z	285.1 (13.37%)	531.9 (45.83%)	102.3 (20.76%)	74.4 (10.02%)	1072.2 (10.02%)	-
HN-WSB-Z-Cu(II)	285.2 (14.06%)	532.3 (39.13%)	102.5 (20.27%)	74.9 (11.20%)	1072.5 (1.50%)	(13.84%)
GZ	285.1 (16.46%)	531.9 (50.86%)	102.2 (16.74%)	74.2 (8.03%)	1072.3 (7.90%)	-
GZ-Cu(II)	285.4 (17.56%)	532.5 (42.26%)	102.7 (17.03%)	75.2 (10.45%)	1072.9 (0.84%)	(11.86%)

As shown in Figure S5a,c, the Cu was observed and the peak areas of Na decreased significantly in HN-WSB-Z-Cu(II) and GZ-Cu(II), while the relative contents of the adsorption Cu were 13.84% and 11.86%, and the Na were reduced approximately 8.52% and 7.06%, respectively (Table 2), suggesting ion exchange in the Cu(II) adsorption. In the Cu 2p spectra of HN-WSB-Z-Cu(II) and GZ-Cu(II), shown in Figure S5b,d, the peaks at 935.46 (2p3/2) and 955.37 eV (2p1/2) are assigned to $Cu(OH)_2$ [55], revealing the complexation of copper ions with -OH [17].

The Si 2p spectra shown in Figure S6 fitted well with three peaks, at 100.9–101.1 eV, 102.2–102.6 eV and 103.4–103.9 eV associated to the Si-C, Si-O-Si and Si-OH, respectively [56–58]. Si-C relative content in the composite FAUs was significantly increased, mainly due to the formation of Si-C by the bonding of carbon materials and silicon oxides. This is indicative of direct interaction between FAU and the biochar/GO matrix. The relative content of Si-OH was also enhanced, providing the main sites for copper-ion adsorption [59], and the relative contents of Si-OH of composite FAUs were as follows: HN-WSB-Z (20.20%) > H-WSB-Z (13.88%) > GZ (13.03%) > WSB-Z (11.55%) > N-WSB-Z (9.47%) > Z (7.11%).

3.2. Batch Adsorption Experiments

Figure 5a,b show that the Cu(II) adsorption capacities of all the composite FAUs increased, which may have been due to the enhanced mesopore volume, ion-exchange sites and Si-OH. As is evident from Table 1 and Figure 1d,h, following the adsorption of Cu(II), the V_{mic} of HN-WSB-Z and GZ decreased sharply, while the V_{mes} decreased slightly, indicating that the enhanced mesopores, as mass transfer channel, significantly promoted the Cu(II) transfer process. The Cu(II) adsorption capacities were as follows: HN-WSB-Z (118.96 mg/g) > H-WSB-Z (108.02 mg/g) > GZ (106.70 mg/g) > WSB-Z (104.75 mg/g) > N-WSB-Z (95.45 mg/g) > Z (84.10 mg/g), which was the same order as that observed with the Si-OH relative contents. HN-WSB-Z showed the maximal Cu(II) adsorption capacity, attributable to the highest relative content of Si-OH, V_{mes} and ion-exchange sites.

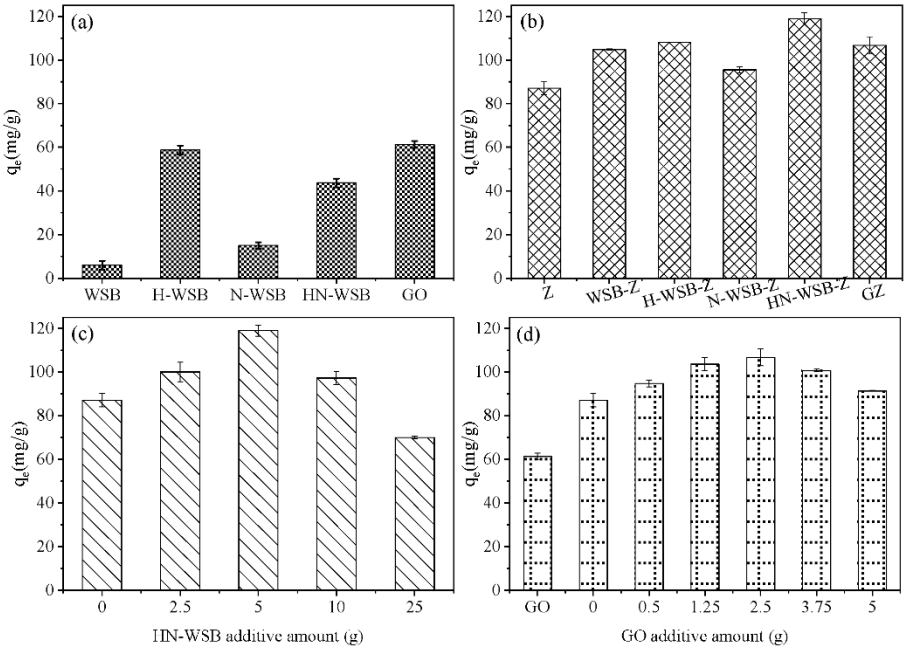

Figure 5. Cu(II) adsorption capacities of biochar and GO (**a**), Z and composite FAUs (**b**), composite FAUs with different additive amount of HN-WSB (**c**) and GO (**d**) (conditions: T = 298 K, t = 180 min, C_0 = 20 mg/L, dosage = 0.2 g/L).

The Cu(II) adsorption capacities of the prepared *x*HN-WSB-Z and *x*GZ are presented in Figure 5c,d. When the weight ratios (*x*) were changed from 0 to 5 and 0 to 2.5, the adsorption capacities increased obviously, from 84.10 mg/g to 118.96 mg/g and 106.70 mg/g, respectively; however, with the change in *x* from 5 to 25 and 2.5 to 5, absorption capacities decreased to 69.95 mg/g and 91.34 mg/g, respectively. 5HN-WSB-Z (i.e., HN-WSB-Z) and 2.5GZ (i.e., GZ) showed the best adsorption capacities, at 118.96 mg/g and 106.70 mg/g, respectively. This is mainly because 5HN-WSB-Z and 2.5GZ have abundant mesopores (shown in Table 1 and Figure 1), which could promote the physical and chemical capture and transport of copper ions.

3.3. Adsorption Isotherms and Kinetics

3.3.1. Adsorption Isotherms

The Langmuir and Freundlich models were applied for the nonlinear fitting of Cu(II) adsorption capacities to equilibrium concentrations by GZ and HN-WSB-Z (Figure 6a). The equation of each model is presented in Equations (1) and (2):

$$\text{Langmuir}: \frac{C_e}{q_e} = \frac{1}{q_{max}K_L} + \frac{C_e}{q_{max}} \quad (1)$$

$$\text{Freundlich}: \ln q_e = \ln K_F + \frac{1}{n}\ln C_e \quad (2)$$

where C_e (mg/L), q_e (mg/g) and q_{max} (mg/g) are the equilibrium Cu(II) concentration in the solution, the equilibrium and the maximum adsorption capacity, respectively. K_L ((mg/g)/(L/mg)$^{1/n}$), K_F (L/mg) and n are the Langmuir constant, and the Freundlich constants are related to the adsorption capacity and adsorption intensity, respectively.

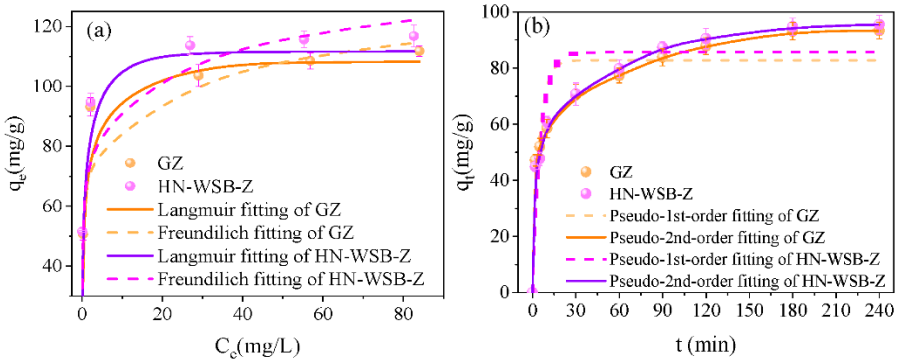

Figure 6. Cu(II) adsorption isotherm fitting curves of GZ and HN-WSB-Z (**a**); nonlinear fitting of pseudo-1st-order and pseudo-2nd-order for Cu(II) adsorption by GZ and HN-WSB-Z (**b**). (Conditions: T = 298 K, t = 180 min, C_0 = 20 mg/L, dosage = 0.2 g/L).

The fitting parameters are summarized in Table S2. The q_e increased significantly with C_e until C_e had reached 20 mg/g, and the two models provided a good fitting for the experimental data, with correlation coefficients (R^2) higher than 0.81. In contrast, the experimental data for Cu(II) correlated better with the Langmuir model (Figure 6a), and the R^2 values reached 0.9889 (GZ) and 0.9927 (HN-WSB-Z). Therefore, it is evident that the adsorption of Cu(II) into GZ and HN-WSB-Z adhered to the Langmuir model via mainly monolayer adsorption [17,60]. The maximum adsorption values for Cu(II) were 108.68 mg/g and 115.65 mg/g by GZ with HN-WSB-Z at 298 K, which was relatively excellent compared to the other adsorbents (Table 3).

Table 3. Comparison of maximum Cu(II) adsorption capacities (q_{max}) by various adsorbents.

Adsorbents	Temperature (K)	q_{max} (mg·g^{-1})	References
HN-WSB-Z	298	115.65	This work
GZ	298	108.68	This work
NaP zeolite	298	62.30	[59]
Commercial zeolite	298	39.15	[17]
FAU zeolite	298	94.46	[17]
Humic acid-immobilized surfactant-modified zeolite	298	19.80	[61]
Modified montmorillonite	288	29.15	[62]
Granular sludge-clay	298	2.76	[63]
Pig bone char with amino functionalization	303	30.50	[64]
Willow wood	298	11.30	[65]
Willow wood biochar	298	12.20	[65]
Cattle manure	298	21.40	[65]
Cattle manure biochar	298	14.70	[65]
Titanate nanocomposite	293	13.80	[66]

3.3.2. Adsorption Kinetics

The time-dependent Cu(II) adsorption capacities of GZ and HN-WSB-Z are plotted in Figure 6b. GZ and HN-WSB-Z both exhibited a rapid uptake of Cu(II) during the initial 10 min, achieving removal rates of 56.37% and 58.46%, respectively. Subsequently, the adsorption rates gradually decreased and adsorption equilibrium was approached at approximately 180 min, with removal rate and the adsorption capacity reaching 89.95–91.83% and 93.21–94.74 mg/g, respectively.

The pseudo-first-order and pseudo-second-order kinetics models were applied for the adsorption data fitting of Cu(II) by GZ and HN-WSB-Z (Figure 6b). The equation of each model is presented in Equations (3) and (4):

$$\text{Pseudo-1st-order}: \ \ln(q_e - q_t) = \ln q_e - K_1 t \quad (3)$$

$$\text{Pseudo-2nd-order}: \frac{t}{q_t} = \frac{1}{K_2 {q_e}^2} + \frac{1}{q_e} t \quad (4)$$

where q_t is the adsorbed amounts of Cu(II) at time t (min), while K_1 (min^{-1}) and K_2 (g (mg min)$^{-1}$) are the rate constants for the two models, respectively.

The nonlinear fitting of pseudo-first-order and pseudo-second-order models for the Cu(II) adsorption process by GZ and HN-WSB-Z are illustrated in Figure 6b, and the relevant parameters calculated from the models are listed in Table S2. Based on the nonlinear fitting curve and R^2 values, the pseudo-second-order model provided a suitable description for the Cu(II) adsorption by GZ and HN-WSB-Z. The GZ and HN-WSB-Z theoretical calculation adsorption capacities ($q_{e,cal}$) for Cu(II) obtained from the pseudo-second-order model were 95.52 mg/g and 96.50 mg/g, respectively, which are close to the experimental values of 93.21mg/g and 94.74 mg/g, respectively.

3.4. Selective Adsorption Capacity

The presence of other metal ions (such as Ca(II), Mn(II), Ni(II), Co(II) and Mg(II)), which are generally also present in wastewater, could potentially alter the Cu(II) removal efficiency of GZ and HN-WSB-Z. Therefore, the adsorption capacities of GZ and HN-WSB-Z in single presented solutions of Cu(II), Ca(II), Mn(II), Ni(II), Co(II) and Mg(II), and Cu(II)-containing bimetal-ion solutions and their coexisting solutions were also investigated in this study. As shown in Figure 7a,b, the adsorption capacities of GZ and HN-WSB-Z for various metal ions were found to be in the following order: Mg(II) < Co(II) < Ni(II) < Ca(II), Mn(II) < Cu(II). GZ and HN-WSB-Z exhibited excellent adsorption capacities for Cu(II), which were at least 1.78 and 1.75 times that of Mn(II) and up to 3.25 and 9.44 times that of Mg(II).

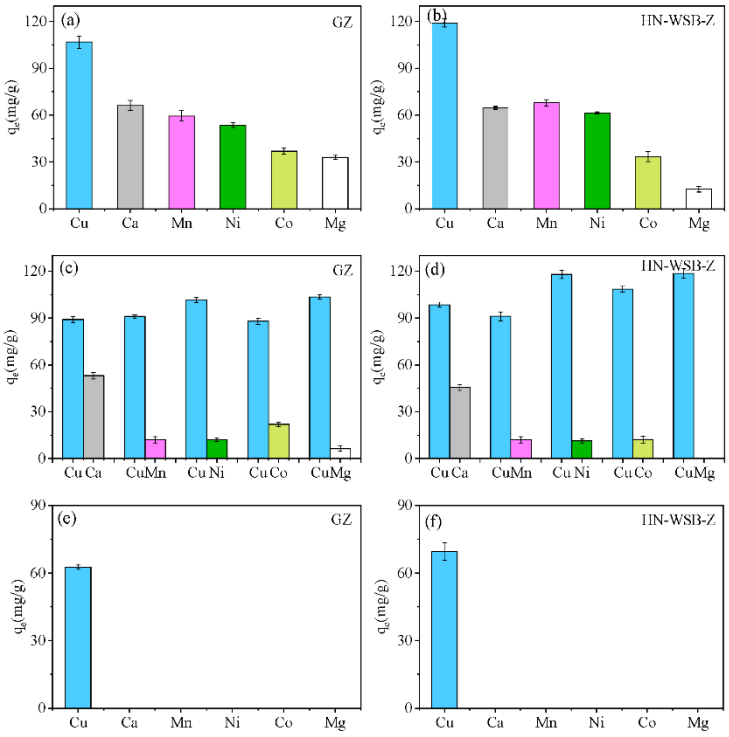

Figure 7. Adsorption capacities of GZ and HN-WSB-Z on Cu(II), Ca(II), Mn(II), Ni(II), Co(II) and Mg(II) in single presented solution (**a**,**b**), Cu(II)-containing two-component metal-ion solution (**c**,**d**), multicomponent metal-ion coexisting solution (**e**,**f**). (Conditions: T = 298 K, t = 180 min, C_0 = 20 mg/L, dosage = 0.2 g/L).

The adsorptive selectivities of GZ and HN-WSB-Z for each metal ion from the coexisting solutions were evaluated by Equations (5) and (6) [67]:

$$\alpha_k^i = \alpha_j^i \times \alpha_k^j \qquad \left(\alpha_j^i = \frac{q_i C_j}{C_i q_j} = \frac{y_i x_j}{x_i y_j}\right) \tag{5}$$

$$x_i = \frac{C_i}{\sum_{k=1}^{m} C_k}, \quad x_j = \frac{C_j}{\sum_{k=1}^{m} C_k}, \quad y_i = \frac{x_i}{\sum_{k=i}^{n} (x_i \alpha_i{}^k)}, \quad y_j = \frac{x_j}{\sum_{k=j}^{n} (x_j \alpha_j{}^k)} \tag{6}$$

where α_k^i is the separation factor of i with respect to ion k; q and C are the equivalent solid-phase and liquid-phase concentrations (mg/L) for ions i and j, respectively; x and y are the liquid-phase and the solid-phase equivalent fractions or mole fractions of i and j, respectively; i represents the counterion; and j is the presaturant ion.

As can be seen from Figure 7c,d, GZ and HN-WSB-Z exhibited a high selectivity toward Cu(II) in the Cu(II)-containing two-component metal-ion solutions of at least 1.68 and 2.16 times that of other metal ions, some of which, such as Mg(II), were not adsorbed at all. In particular, GZ and HN-WSB-Z showed outstanding selectivity by adsorbing only Cu(II) in the multicomponent metal-ion coexisting solution, despite the existence of multiple interfering ions in the solution (Figure 7e,f), with the separation factor (Table S3) up to 41.44). These results suggest that biochar or GO composite FAUs offer good potential as a practically applicable adsorbent for Cu(II) removal.

3.5. Reusability of Composite FAU

The reusability of the HN-WSB-Z was determined via regeneration with NaCl (saturated solution), CH_3COONa (2 mol/L) and H_2O (333 K). The results showed that NaCl and CH_3COONa were effective elution agents for Cu(II) desorption from HN-WSB-Z (Figure 8). After four adsorption–desorption cycles in H_2O, the removal of Cu(II) by HN-WSB-Z was approximately 32%, indicating that the adsorption of Cu(II) is not effective at high temperatures and that physical adsorption is not dominant in the process of adsorption. The decreased adsorption capacity of Cu(II) by HN-WSB-Z after hot-water regeneration was related to the incomplete elution of copper ions on the HN-WSB-Z, which is attributed to the fact that a large number of copper ions occupy the active sites by forming stable chemical bonds with the HN-WSB-Z through ion exchange or complexation. However, after four adsorption–desorption cycles, the adsorption capacity of HN-WSB-Z regenerated with NaCl or CH_3COONa remained as high at 94–95%. Both of the two sodium salts provided excellent regeneration effects on HN-WSB-Z, and their regeneration performance was better than that of pure FAU [17]. The effective regeneration of HN-WSB-Z by sodium salts suggests that ion exchange dominates the adsorption process. The above results show that HN-WSB-Z has excellent regenerability and is a promising adsorbent for industrial applications.

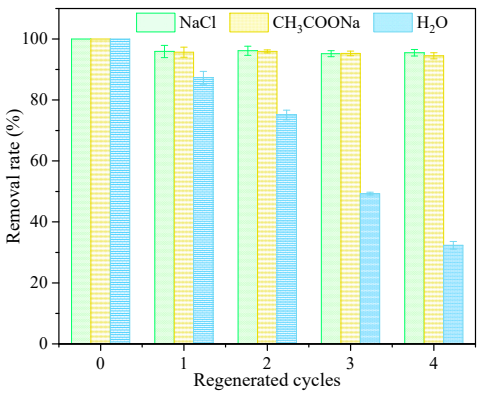

Figure 8. Reusability of composite FAU (HN-WSB-Z) for Cu(II) removal. (Conditions: T = 298 K, t = 180 min, C_0 = 10 mg/L, dosage = 0.2 g/L).

3.6. Mechanism of Cu(II) Removal by the Composite FAUs

The BET results showed that composite FAUs with a highly mesoporous structure exhibited the physical capture of Cu(II). The FTIR analysis revealed that the Cu(II) adsorption process was related to -OH, which was also confirmed by XPS, suggesting -OH complexation with Cu(II). Moreover, XPS results also showed ion exchange to be the main mechanism during the adsorption, which was also confirmed by regeneration studies.

4. Conclusions

This work has presented the hierarchical construction of abundantly mesoporous biochar/GO composite FAUs via a facile hydrothermal method. GO and HN-WSB were shown to significantly improve the mesopore volume and Cu(II) adsorption capacity of the FAU, and the biochar/GO obviously promoted the growth of the FAU crystal, favoring the formation of a T-O-T skeleton structure, ion-exchange site and Si-OH in the FAU. A suitable description for the Cu(II) adsorption process by HN-WSB-Z and GZ was provided by a pseudo-second-order model. The adsorptions of Cu(II) onto HN-WSB-Z and GZ were observed to obey the Langmuir model of mainly monolayer adsorption, with the maximum Cu(II) adsorption values increasing to 115.65 mg/g and 108.68 mg/g, respectively. The adsorption of Cu(II) onto the composite FAUs relies on physical capture, complexation and ion exchange (predominantly). The composite FAUs also showed outstanding selectivity and reusability toward Cu(II), further supporting their potential as promising candidates for wastewater Cu(II) adsorption applications.

Supplementary Materials: The following supporting information can be downloaded at: https://www.mdpi.com/article/10.3390/w14132040/s1, Figure S1: SEM micrograph and the EDS mapping analysis of HN-WSB-Z, GZ and the SEM micrograph of Z; Figure S2: XRD patterns of graphite; Figure S3: FTIR spectra of HN-WSB-Z and HN-WSB-Z-Cu(II) (a), GZ and GZ-Cu(II) (b); Figure S4: XPS wide scan spectra of GO and different biochar (a), GO composite FAU, different biochar composite FAUs and pure FAU (Z) (b); Figure S5: XPS wide scan spectra of HN-WSB-Z (a) and GZ (c), Cu 2p spectrum of HN-WSB-Z-Cu(II) (b) and GZ-Cu(II) (d); Figure S6: Si 2p spectrum of Z (a), WSB-Z (b), H-WSB-Z (c), N-WSB-Z (d), HN-WSB-Z (e) and GZ (f); Table S1: The crystallite dimensions of the main lattice planes of different composite FAUs; Table S2: Kinetics and isothermal adsorption fitting data of HN-WSB-Z and GZ; Table S3: α_k^i of GZ and HN-WSB-Z on multicomponent bivalent metal ions.

Author Contributions: Conceptualization, supervision, W.J.; methodology, resources, J.G.; validation, S.W. and S.D.; formal analysis, investigation, writing—original draft, Y.C. All authors have read and agreed to the published version of the manuscript.

Funding: This research was funded by Talent Introduction Program of Xihua University, grant number Z202117.

Institutional Review Board Statement: Not applicable.

Informed Consent Statement: Not applicable.

Data Availability Statement: The data presented in this study are available in [A mesoporous faujasite prepared by space-confined method for highly effective selectivity of copper ions].

Conflicts of Interest: The authors declare no conflict of interest.

References

1. Elshkaki, A.; Graedel, T.E.; Ciacci, L.; Reck, B. Copper demand, supply, and associated energy use to 2050. *Glob. Environ. Chang.* **2016**, *39*, 305–315. [CrossRef]
2. Kang, J.-K.; Lee, S.-C.; Kim, S.-B. Enhancement of selective Cu(II) sorption through preparation of surface-imprinted mesoporous silica SBA-15 under high molar concentration ratios of chloride and copper ions. *Microporous Mesoporous Mater.* **2018**, *272*, 193–201. [CrossRef]
3. Wang, K.; Wang, W.; Li, L.; Li, J.; Wei, L.; Chi, W.; Hong, L.; Zhao, Q.; Jiang, J. Seasonal concentration distribution of PM1.0 and PM2.5 and a risk assessment of bound trace metals in Harbin, China: Effect of the species distribution of heavy metals and heat supply. *Sci. Rep.* **2020**, *10*, 8160. [CrossRef] [PubMed]

4. Mazurek, R.; Kowalska, J.; Gąsiorek, M.; Zadrożny, P.; Józefowska, A.; Zaleski, T.; Kępka, W.; Tymczuk, M.; Orłowska, K. Assessment of heavy metals contamination in surface layers of Roztocze National Park forest soils (SE Poland) by indices of pollution. *Chemosphere* **2017**, *168*, 839–850. [CrossRef] [PubMed]
5. Zhang, W.; Liu, M.; Li, C. Soil heavy metal contamination assessment in the Hun-Taizi River watershed, China. *Sci. Rep.* **2020**, *10*, 8730. [CrossRef]
6. Allafta, H.; Opp, C. Spatio-temporal variability and pollution sources identification of the surface sediments of Shatt Al-Arab River, Southern Iraq. *Sci. Rep.* **2020**, *10*, 6979. [CrossRef]
7. Harikrishnan, N.; Ravisankar, R.; Chandrasekaran, A.; Gandhi, M.S.; Kanagasabapathy, K.; Prasad, M.; Satapathy, K. Assessment of Heavy Metal Contamination in Marine Sediments of East Coast of Tamil Nadu Affected by Different Pollution Sources. *Mar. Pollut. Bull.* **2017**, *121*, 418–424. [CrossRef]
8. Mirbagheri, S.; Hosseini, S. Pilot plant investigation on petrochemical wastewater treatmentfor the removal of copper and chromium with the objective of reuse. *Desalination* **2005**, *171*, 85–93. [CrossRef]
9. Huisman, J.L.; Schouten, G.; Schultz, C. Biologically produced sulphide for purification of process streams, effluent treatment and recovery of metals in the metal and mining industry. *Hydrometallurgy* **2006**, *83*, 106–113. [CrossRef]
10. Villa-Gomez, D.; Ababneh, H.; Papirio, S.; Rousseau, D.; Lens, P. Effect of sulfide concentration on the location of the metal precipitates in inversed fluidized bed reactors. *J. Hazard. Mater.* **2011**, *192*, 200–207. [CrossRef]
11. Camarillo, R.; Llanos, J.; García-Fernández, L.; Perez, A.; Cañizares, P. Treatment of copper (II)-loaded aqueous nitrate solutions by polymer enhanced ultrafiltration and electrodeposition. *Sep. Purif. Technol.* **2010**, *70*, 320–328. [CrossRef]
12. Cifuentes, L.; García, I.; Arriagada, P.; Casas, J. The use of electrodialysis for metal separation and water recovery from CuSO4–H_2SO_4–Fe solutions. *Sep. Purif. Technol.* **2009**, *68*, 105–108. [CrossRef]
13. Galal, A.; Zaki, M.M.; Atta, N.F.; Samaha, S.; Nasr, H.; Attia, N.F. Electroremoval of copper ions from aqueous solutions using chemically synthesized polypyrrole on polyester fabrics. *J. Water Process Eng.* **2021**, *43*, 102287. [CrossRef]
14. Khan, J.; Lin, S.; Nizeyimana, J.C.; Wu, Y.; Wang, Q.; Liu, X. Removal of copper ions from wastewater via adsorption on modified hematite (α-Fe_2O_3) iron oxide coated sand. *J. Clean. Prod.* **2021**, *319*, 128687. [CrossRef]
15. Darweesh, M.A.; Elgendy, M.Y.; Ayad, M.I.; Ahmed, A.M.; Elsayed, N.; Hammad, W. Adsorption isotherm, kinetic, and optimization studies for copper (II) removal from aqueous solutions by banana leaves and derived activated carbon. *S. Afr. J. Chem. Eng.* **2022**, *40*, 10–20. [CrossRef]
16. Joseph, I.V.; Tosheva, L.; Doyle, A.M. Simultaneous removal of Cd(II), Co(II), Cu(II), Pb(II), and Zn(II) ions from aqueous solutions via adsorption on FAU-type zeolites prepared from coal fly ash. *J. Environ. Chem. Eng.* **2020**, *8*, 103895. [CrossRef]
17. Chen, Y.; Armutlulu, A.; Sun, W.; Jiang, W.; Jiang, X.; Lai, B.; Xie, R. Ultrafast removal of Cu(II) by a novel hierarchically structured faujasite-type zeolite fabricated from lithium silica fume. *Sci. Total Environ.* **2020**, *714*, 136724. [CrossRef] [PubMed]
18. Liu, Y.; Wang, G.; Luo, Q.; Li, X.; Wang, Z. The thermodynamics and kinetics for the removal of copper and nickel ions by the zeolite Y synthesized from fly ash. *Mater. Res. Express* **2018**, *6*, 025001. [CrossRef]
19. Khanmohammadi, H.; Bayati, B.; Shahrouzi, J.R.; Babaluo, A.-A.; Ghorbani, A. Molecular simulation of the ion exchange behavior of Cu^{2+}, Cd^{2+} and Pb^{2+} ions on different zeolites exchanged with sodium. *J. Environ. Chem. Eng.* **2019**, *7*, 103040. [CrossRef]
20. Bai, R.; Song, Y.; Li, Y.; Yu, J. Creating Hierarchical Pores in Zeolite Catalysts. *Trends Chem.* **2019**, *1*, 601–611. [CrossRef]
21. Reinoso, D.; Adrover, M.; Pedernera, M. Green synthesis of nanocrystalline faujasite zeolite. *Ultrason. Sonochem.* **2018**, *42*, 303–309. [CrossRef] [PubMed]
22. Pérez-Ramírez, J.; Christensen, C.H.; Egeblad, K.; Christensen, C.H.; Groen, J.C. Hierarchical zeolites: Enhanced utilisation of microporous crystals in catalysis by advances in materials design. *Chem. Soc. Rev.* **2008**, *37*, 2530–2542. [CrossRef] [PubMed]
23. Murzin, D.; Salmi, T. Mass transfer and catalytic reactions. In *Catalytic Kinetics*; Elsevier Science: Amsterdam, The Netherlands, 2005; pp. 341–418. [CrossRef]
24. Valiullin, R.; Kärger, J. The Impact of Mesopores on Mass Transfer in Nanoporous Materials: Evidence of Diffusion Measurement by NMR. *Chem. Ing. Tech.* **2011**, *83*, 166–176. [CrossRef]
25. Inayat, A.; Knoke, I.; Spiecker, E.; Schwieger, W. Assemblies of Mesoporous FAU-Type Zeolite Nanosheets. *Angew. Chem. Int. Ed.* **2012**, *51*, 1962–1965. [CrossRef] [PubMed]
26. Wang, Z.; Dornath, P.; Chang, C.-C.; Chen, H.; Fan, W. Confined synthesis of three-dimensionally ordered mesoporous-imprinted zeolites with tunable morphology and Si/Al ratio. *Microporous Mesoporous Mater.* **2013**, *181*, 8–16. [CrossRef]
27. Derouane, E.G.; André, J.-M.; Lucas, A.A. A simple van der waals model for molecule-curved surface interactions in molecular-sized microporous solids. *Chem. Phys. Lett.* **1987**, *137*, 336–340. [CrossRef]
28. Wang, J.; Yang, M.; Zhang, J.; Zhang, S.; Wang, X.; Fu, K.; Wang, M.; Shang, W.; Chen, H.; Ma, X. Fabrication of BEA/MFI zeolite nanocomposites by confined space synthesis. *Mater. Chem. Phys.* **2018**, *207*, 167–174. [CrossRef]
29. Chen, H.; Lee, P.-S.; Zhang, X.; Lu, D. Structure replication and growth development of three-dimensionally ordered mesoporous-imprinted zeolites during confined growth. *J. Mater. Res.* **2013**, *28*, 1356–1364. [CrossRef]
30. Hummers, W.S., Jr.; Offeman, R.E. Preparation of Graphitic Oxide. *J. Am. Chem. Soc.* **1958**, *80*, 1339. [CrossRef]
31. Li, L.; Quinlivan, P.A.; Knappe, D. Effects of activated carbon surface chemistry and pore structure on the adsorption of organic contaminants from aqueous solution. *Carbon* **2002**, *40*, 2085–2100. [CrossRef]
32. Dimiev, A.M.; Tour, J.M. Mechanism of Graphene Oxide Formation. *ACS Nano* **2014**, *8*, 3060–3068. [CrossRef] [PubMed]

33. Marcano, D.C.; Kosynkin, D.V.; Berlin, J.M.; Sinitskii, A.; Sun, Z.; Slesarev, A.; Alemany, L.B.; Lu, W.; Tour, J.M. Improved Synthesis of Graphene Oxide. *ACS Nano* **2010**, *4*, 4806–4814. [CrossRef] [PubMed]
34. Liu, Y.; Yan, C.; Qiu, X.; Li, D.; Wang, H.; Alshameri, A. Preparation of faujasite block from fly ash-based geopolymer via in-situ hydrothermal method. *J. Taiwan Inst. Chem. Eng.* **2016**, *59*, 433–439. [CrossRef]
35. Du, T.; Adeleye, A.S.; Zhang, T.; Yang, N.; Hao, R.; Li, Y.; Song, W.; Chen, W. Effects of ozone and produced hydroxyl radicals on the transformation of graphene oxide in aqueous media. *Environ. Sci. Nano* **2019**, *6*, 2484–2494. [CrossRef]
36. Jiang, Y.; Raliya, R.; Liao, P.; Biswas, P.; Fortner, J.D. Graphene oxides in water: Assessing stability as a function of material and natural organic matter properties. *Environ. Sci. Nano* **2017**, *4*, 1484–1493. [CrossRef]
37. Lian, W.; Yang, L.; Joseph, S.; Shi, W.; Bian, R.; Zheng, J.; Li, L.; Shan, S.; Pan, G. Utilization of biochar produced from invasive plant species to efficiently adsorb Cd (II) and Pb (II). *Bioresour. Technol.* **2020**, *317*, 124011. [CrossRef]
38. Qian, K.; Kumar, A.; Patil, K.; Bellmer, D.; Wang, D.; Yuan, W.; Huhnke, R.L. Effects of biomass feedstocks and gasification conditions on the physiochemical properties of char. *Energies* **2013**, *6*, 3972–3986. [CrossRef]
39. Tseng, H.-H.; Wey, M.-Y. Effects of acid treatments of activated carbon on its physiochemical structure as a support for copper oxide in DeSO2 reaction catalysts. *Chemosphere* **2006**, *62*, 756–766. [CrossRef]
40. Fanning, P.E.; Vannice, M. A DRIFTS study of the formation of surface groups on carbon by oxidation. *Carbon* **1993**, *31*, 721–730. [CrossRef]
41. Huang, Z.; Hu, L.; Tang, W.; Guo, Y.; Dai, J. Effects of biochar aging on adsorption behavior of phenanthrene. *Chem. Phys. Lett.* **2020**, *759*, 137948. [CrossRef]
42. Barathi, M.; Kumar, A.S.K.; Kumar, C.U.; Rajesh, N. Graphene oxide–aluminium oxyhydroxide interaction and its application for the effective adsorption of fluoride. *RSC Adv.* **2014**, *4*, 53711–53721. [CrossRef]
43. Kong, Q.; Preis, S.; Li, L.; Luo, P.; Wei, C.; Li, Z.; Hu, Y.; Wei, C. Relations between metal ion characteristics and adsorption performance of graphene oxide: A comprehensive experimental and theoretical study. *Sep. Purif. Technol.* **2019**, *232*, 115956. [CrossRef]
44. García-Villén, F.; Flores-Ruíz, E.; Verdugo-Escamilla, C.; Huertas, F.J. Hydrothermal synthesis of zeolites using sanitary ware waste as a raw material. *Appl. Clay Sci.* **2018**, *160*, 238–248. [CrossRef]
45. Yang, L.; Qian, X.; Yuan, P.; Bai, H.; Miki, T.; Men, F.; Li, H.; Nagasaka, T. Green synthesis of zeolite 4A using fly ash fused with synergism of NaOH and Na_2CO_3. *J. Clean. Prod.* **2019**, *212*, 250–260. [CrossRef]
46. Pal, P.; Das, J.K.; Das, N.; Bandyopadhyay, S. Synthesis of NaP zeolite at room temperature and short crystallization time by sonochemical method. *Ultrason. Sonochem.* **2013**, *20*, 314–321. [CrossRef]
47. Sayehi, M.; Garbarino, G.; Delahay, G.; Busca, G.; Tounsi, H. Synthesis of high value-added Na–P1 and Na-FAU zeolites using waste glass from fluorescent tubes and aluminum scraps. *Mater. Chem. Phys.* **2020**, *248*, 122903. [CrossRef]
48. Abdelrahman, E.A.; El-Reash, Y.A.; Youssef, H.M.; Kotp, Y.H.; Hegazey, R. Utilization of rice husk and waste aluminum cans for the synthesis of some nanosized zeolite, zeolite/zeolite, and geopolymer/zeolite products for the efficient removal of Co(II), Cu(II), and Zn(II) ions from aqueous media. *J. Hazard. Mater.* **2021**, *401*, 123813. [CrossRef]
49. Koohsaryan, E.; Anbia, M. Facile and rapid synthesis of highly crystalline mesoporous zeolite FAU. *Mater. Lett.* **2019**, *236*, 390–393. [CrossRef]
50. Li, Y.; Zhang, K.; Chen, Y.; Zhang, Y.; Liang, X.; Han, L.; Li, X.; Han, P. Highly efficient synthesis of high-silica SSZ-13 zeolite by interzeolite transformation of L zeolite at higher temperature. *J. Solid State Chem.* **2021**, *293*, 121769. [CrossRef]
51. Souza, I.M.; Borrego-Sánchez, A.; Sainz-Díaz, C.I.; Viseras, C.; Pergher, S.B. Study of Faujasite zeolite as a modified delivery carrier for isoniazid. *Mater. Sci. Eng. C* **2021**, *118*, 111365. [CrossRef]
52. Benaliouche, F.; Boucheffa, Y.; Thibault-Starzyk, F. In situ FTIR studies of propene adsorption over Ag- and Cu-exchanged Y zeolites. *Microporous Mesoporous Mater.* **2012**, *147*, 10–16. [CrossRef]
53. Cheng, Y.; Xu, L.; Liu, C. NaP1 zeolite synthesized via effective extraction of Si and Al from red mud for methylene blue adsorption. *Adv. Powder Technol.* **2021**, *32*, 3904–3914. [CrossRef]
54. Hu, G.; Duan, X.; Yang, J.; Yang, C.; Liu, Q.; Ren, S.; Li, J.; Teng, L.; Liu, W. A novel conversion of Ti-bearing blast furnace slag into Ti-containing zeolites: Comparison study between FAU and MFI type zeolites. *Adv. Powder Technol.* **2022**, *33*, 103559. [CrossRef]
55. McIntyre, N.S.; Sunder, S.; Shoesmith, D.W.; Stanchell, F.W. Chemical information from XPS—Applications to the analysis of electrode surfaces. *J. Vac. Sci. Technol.* **1981**, *18*, 714–721. [CrossRef]
56. Post, P.; Wurlitzer, L.; Maus-Friedrichs, W.; Weber, A.P. Characterization and Applications of Nanoparticles Modified in-Flight with Silica or Silica-Organic Coatings. *Nanomaterials* **2018**, *8*, 530. [CrossRef]
57. Barr, T.L. An XPS study of Si as it occurs in adsorbents, catalysts, and thin films. *Appl. Surf. Sci.* **1983**, *15*, 1–35. [CrossRef]
58. Gustus, R.; Gruber, W.; Wegewitz, L.; Geckle, U.; Prang, R.; Kübel, C.; Schmidt, H.; Maus-Friedrichs, W. Decomposition of amorphous Si2C by thermal annealing. *Thin Solid Film* **2014**, *552*, 232–240. [CrossRef]
59. Pu, X.; Yao, L.; Yang, L.; Jiang, W.; Jiang, X. Utilization of industrial waste lithium-silicon-powder for the fabrication of novel nap zeolite for aqueous Cu(II) removal. *J. Clean. Prod.* **2020**, *265*, 121822. [CrossRef]
60. Wang, Y.-Y.; Liu, Y.-X.; Lu, H.-H.; Yang, R.-Q.; Yang, S.-M. Competitive adsorption of Pb(II), Cu(II), and Zn(II) ions onto hydroxyapatite-biochar nanocomposite in aqueous solutions. *J. Solid State Chem.* **2018**, *261*, 53–61. [CrossRef]
61. Lin, J.; Zhan, Y.; Zhu, Z. Adsorption characteristics of copper (II) ions from aqueous solution onto humic acid-immobilized surfactant-modified zeolite. *Colloids Surfaces A Physicochem. Eng. Asp.* **2011**, *384*, 9–16. [CrossRef]

62. Chu, Y.; Khan, M.A.; Wang, F.; Xia, M.; Lei, W.; Zhu, S. Kinetics and equilibrium isotherms of adsorption of Pb(II) and Cu(II) onto raw and arginine-modified montmorillonite. *Adv. Powder Technol.* **2019**, *30*, 1067–1078. [CrossRef]
63. Du, X.; Cui, S.; Fang, X.; Wang, Q.; Liu, G. Adsorption of Cd(II), Cu(II), and Zn(II) by granules prepared using sludge from a drinking water purification plant. *J. Environ. Chem. Eng.* **2020**, *8*, 104530. [CrossRef]
64. Liu, Y.; Xu, J.; Cao, Z.; Fu, R.; Zhou, C.; Wang, Z.; Xu, X. Adsorption behavior and mechanism of Pb(II) and complex Cu(II) species by biowaste-derived char with amino functionalization. *J. Colloid Interface Sci.* **2020**, *559*, 215–225. [CrossRef] [PubMed]
65. Wang, S.; Kwak, J.-H.; Islam, S.; Naeth, M.A.; El-Din, M.G.; Chang, S.X. Biochar surface complexation and Ni(II), Cu(II), and Cd(II) adsorption in aqueous solutions depend on feedstock type. *Sci. Total Environ.* **2020**, *712*, 136538. [CrossRef]
66. Wang, A.; Si, Y.; Yin, H.; Chen, J.; Huo, J. Synthesis of Na-, Fe-, and Mg-containing titanate nanocomposites starting from ilmenite and NaOH and adsorption kinetics, isotherms, and thermodynamics of Cu(II), Cd(II), and Pb(II) cations. *Mater. Sci. Eng. B* **2019**, *249*, 114411. [CrossRef]
67. Luo, X.; Zhang, K.; Luo, J.; Luo, S.; Crittenden, J. Capturing lithium from wastewater using a fixed bed packed with 3-D MnO2 ion cages. *Environ. Sci. Technol.* **2016**, *50*, 13002–13012. [CrossRef]